

On the Coherency of Ocean and Land Surface Specular Scattering for GNSS-R and Signals of Opportunity Systems

Ahmed M. Balakhder¹, *Member, IEEE*, Mohammad M. Al-Khaldi¹, *Member, IEEE*,
and Joel T. Johnson¹, *Fellow, IEEE*

Abstract—An analysis of the coherency properties of specular scattering from ocean and land surfaces as observed in global navigation satellite system-reflectometry (GNSS-R) and signals of opportunity systems is presented. This analysis applies existing approximate models for the coherent and incoherent contributions. Approximate expressions are developed for when one component of the return is likely to dominate as a function of surface and observing system properties. The model developed is then applied for sea surface returns, and the relative contribution of the coherent term is expressed as a function of the receiver height, frequency, incidence angle, and wind speed. For L-band spaceborne measurements, it is shown that coherence is expected only for wind speeds less than 2–3 m/s, while for P-band spaceborne measurements, coherence can dominate returns for wind speeds up to 5–7 m/s. For land surface measurements from space, it is shown that the surface rms height needs to be sufficiently low for coherent components to dominate returns. Coherence dominates for roughness values not exceeding a range of 5–7 cm for the L-band and 15–30 cm for the P-band. For the L-band, these conditions over land are likely to be created primarily by inland water bodies. A model for the specular scattering from a water body, including earth curvature effects, is then developed to highlight the strong dependence of the resulting coherent field on the shape of the water body and any offset in its location from the specular point. These results further clarify the significant variability that should be expected in coherent scattering from inland water bodies.

Index Terms—Bistatic systems, coherency, incoherency, random media, rough surface scattering.

I. INTRODUCTION

THE use of the transmissions of existing RF systems (also known as “signals of opportunity” or SoOp) for earth remote sensing is of increasing interest. The transmissions of Global Navigation Satellite System (GNSS), in particular, have been explored for remote sensing applications [1]–[14] in the field known as GNSS-reflectometry (GNSS-R). GNSS-R emphasizes the use of the L-band signals, while other SoOp investigations have used transmitters in *P*, *S*, *K_u*, or other bands [15]–[19]. Both GNSS-R and SoOp measurements

Manuscript received February 25, 2019; revised April 29, 2019 and July 2, 2019; accepted July 28, 2019. (*Corresponding author: Ahmed M. Balakhder.*)

The authors are with the Department of Electrical and Computer Engineering and the ElectroScience Laboratory, The Ohio State University, Columbus, OH 43210 USA (e-mail: balakhder.1@osu.edu).

Color versions of one or more of the figures in this article are available online at <http://ieeexplore.ieee.org>.

Digital Object Identifier 10.1109/TGRS.2019.2935257

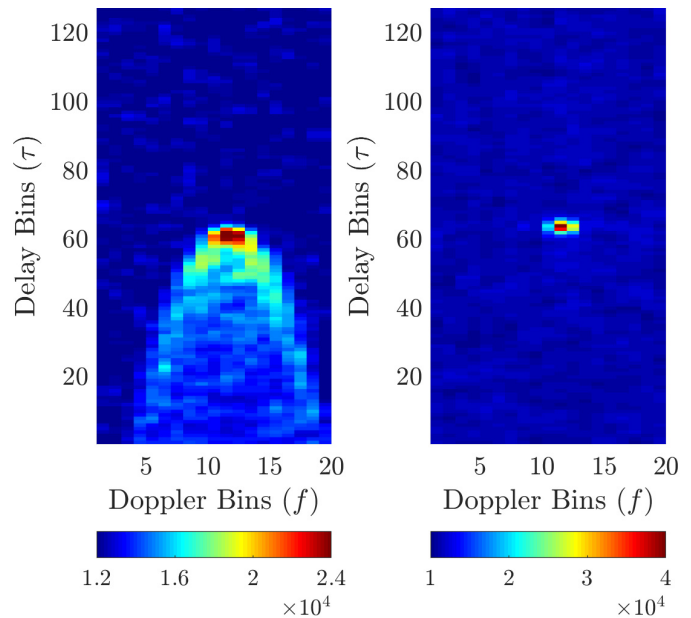


Fig. 1. Example CYGNSS DDMs demonstrating (Left) incoherent and (Right) coherent returns; color scale is in instrument raw counts that are proportional to signal power. Incoherent DDM measured by CYG01 at 23.29°N 42.42°W on DOY 246, 2017 with wind speed estimate ≈ 6 m/s. Coherent DDM measured by CYG03 at 32.427°N 91.011°W on DOY 258, 2018 over the Mississippi River.

for remote sensing are typically performed in a specular scattering geometry because earth-reflected signals have the greatest amplitude at specular scattering. The earth-reflected signals received are then typically used to create delay-Doppler map (DDM) measurements. The DDM maps the power scattered from Earth’s surface as a function of time delay (τ) and Doppler frequency (f) shifts from the specular point on the surface (see Fig. 1).

Over ocean surfaces at the L-band, it is typically assumed that returns are “incoherent” and, therefore, described by the bistatic radar equation [20], [21]. The sea surface specular normalized radar cross section (NRCS) can then be modeled in many cases using the geometric optics’ (GOs) limit of the Kirchhoff approximation for rough surface scattering, which results in the “horseshoe” shape of the DDM shown in Fig. 1 (left). The use of the GO limit requires that the surface rms height is at least a significant fraction of the electromagnetic

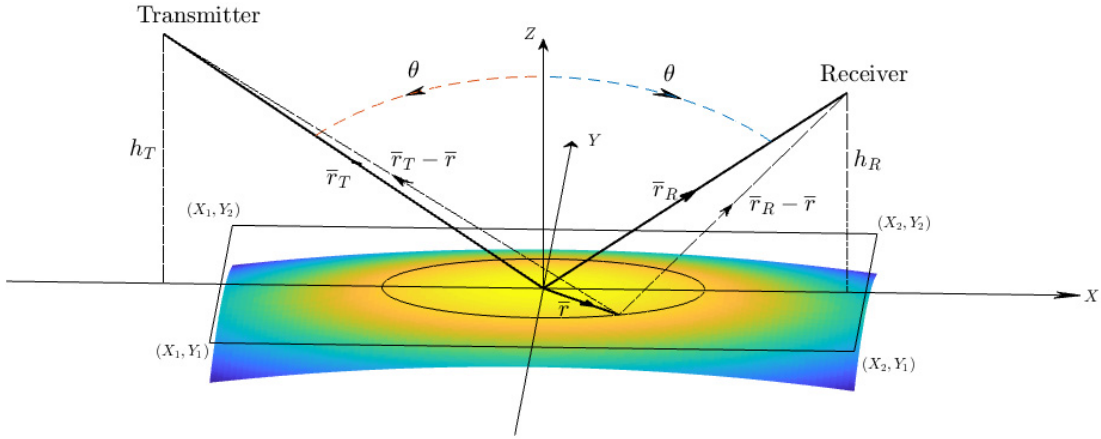


Fig. 2. Bistatic specular scattering geometry.

wavelength, which is typically satisfied at the L-band and higher frequencies except at the lowest wind speeds. When the surface rms height is reduced, the specular scattering can become “coherent,” resulting in a DDM characterized by a sharp response about the specular point [Fig. 1 (right)] whose amplitude in some cases can be many times larger than typical incoherent returns.

This article investigates these coherent returns and develops an approximate model for the relative contributions of coherent and incoherent scattering for sea and land surfaces. It is noted that here “coherence” is defined to be the result of a scattering process in which the fields scattered from a significant portion of the observed Earth surface arrive at the receiver having similar phase shifts and therefore add coherently. The term “coherence” is also used in referring to the coherence time of observed scattered fields, which is not considered in this article, and which also depends on the relative velocities of the transmitter and receiver with respect to the specular region on earth’s surface.

Section II develops the approximate model, and Section III applies it to the specific case of specular scattering from the ocean surface. Section IV then considers land surface coherent scattering and shows that for spaceborne L-band observations, coherent contributions are most likely associated with inland water bodies. Section V then develops a model for inland water body coherent reflections that is examined and later specialized for rectangular water bodies as an example. The results demonstrate the significant fluctuations that can occur due to water body shape and spatial offsets. Section VI presents a concluding discussion of this article’s results.

II. BACKGROUND

Fig. 2 shows the forward scattering geometry of interest. In it, a SoOp transmitter illuminates a specular point on earth’s surface from which the forward scattered fields are observed by a receiver. The transmitter and receiver positions are described by the vectors $\bar{r}_T = r_T \hat{r}_T$ and $\bar{r}_R = r_R \hat{r}_R$, respectively, from the specular point; the coordinate system is defined so that these vectors lie in the xz plane. The forward scattering geometry is defined by the condition $\hat{z} \cdot \hat{r}_T = \hat{z} \cdot \hat{r}_R = \cos \theta$, i.e., the specular reflection condition

is satisfied at the specular point. The DDM produced includes scattering from the specular point as well as other points on earth’s surface at position \bar{r} with respect to the specular point. The example of a spherically curved earth surface truncated over a rectangular boundary between X_1 and X_2 along x and Y_1 and Y_2 along y is also shown in Fig. 2; specular scattering for this particular boundary is explored in greater detail in Section V.

A. Approximation for Coherent Power

A smooth surface will have most of the incident power reflected toward the receiver from the specular point with a peak power that can be many times larger than that arising from incoherent scatter due to the coherent summation of scattered fields that occurs for a flat surface. This “coherent component” is described by the Friis transmission equation (additional information in Section V) modified by a term accounting for the reduction of the reflection coefficient caused by surface roughness

$$P_R^{\text{coh}} = \frac{P_T \lambda^2 G_R G_T}{(4\pi)^2 (r_R + r_T)^2} \cdot |\Re|^2 \cdot Z_f \cdot e^{-4k_0^2 h^2 \cos^2 \theta} \quad (1)$$

where P_R^{coh} is the coherent component of the received power and P_T is the transmitted power. Also G_T and G_R are the transmit and receive antenna gains in the direction of the specular point, and \Re is the surface Fresnel reflectivity for incidence angle θ and the appropriate polarization combination. The exponential term determines the coherent reflection loss (CRL) caused by surface roughness, which in decibels can be written as

$$\text{CRL} = -10 \cdot \log_{10} (e^{-4k_0^2 h^2 \cos^2 \theta}) \quad (2)$$

where $k_0 = (2\pi/\lambda)$ is the electromagnetic wavenumber with λ the electromagnetic wavelength and h is the surface rms height (and h^2 the surface height variance). Finally, an additional term Z_f is included to account for the influence of the area/shape of the smooth surface region relative to the Fresnel zone, as will be further explored in Section V.

The coherent received power is often assumed to arise from the first Fresnel zone area surrounding the specular point,

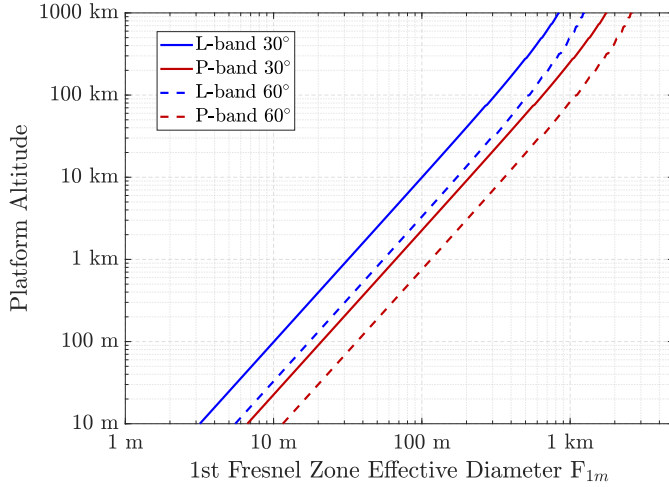


Fig. 3. Orbital altitude versus first fresnel zone average diameter F_{1m} for curved earth.

within which the surface must be sufficiently smooth to cause coherent reflections [i.e., the exponential term in (1) is still appreciable]. For a spherically curved earth surface, the first Fresnel zone is approximately an ellipse having semi-major and semi-minor axes F_{1x} and F_{1y} expressed through

$$F_1 = \sqrt{\frac{\lambda(r_R r_T)}{(r_R + r_T)}} \quad (3)$$

$$D_x = \sqrt{1 + 2 \frac{F_1}{a_{\text{eff}}} \frac{F_1}{\lambda \cos \theta}} \quad (4)$$

$$D_y = \sqrt{1 + 2 \frac{F_1}{a_{\text{eff}}} \frac{F_1 \cos \theta}{\lambda}} \quad (5)$$

$$F_{1x} = \frac{F_1}{D_x \cos \theta} \quad (6)$$

$$F_{1y} = \frac{F_1}{D_y} \quad (7)$$

where a_{eff} is the earth's radius of curvature at the specular point [(27) provides the relevant formulation for these equations]. The terms D_x and D_y represent “divergence factors” caused by earth's curvature. We can further define an “average” Fresnel zone diameter as twice the geometric mean $F_{1m} = 2(F_{1x} F_{1y})^{1/2}$. Fig. 3 plots F_{1m} using (6) and (7) as a function of receiver altitude under the assumption $r_R \ll r_T$ for L- (1.575 GHz) and P- (360 MHz) bands for the incidence angles of 30° and 60°. The results show that the spatial region expected to contribute to coherent returns grows rapidly with receiver orbital altitude and approaches 0.6–3 km in diameter for spaceborne altitudes in the cases shown.

B. Approximation for Incoherent Power

A model describing the incoherent component is also required in order to determine whether the coherent or incoherent terms are dominant. A model given by the bistatic radar equation shown in (8) is adopted. The coherently integrated DDM power received due to incoherent scattering from the

surface can be expressed as [20]–[22]

$$P_R^{\text{inc}}(\tau, f) = \frac{P_T \lambda^2}{(4\pi)^3} \int_A \frac{G_T G_R \sigma^0 \Lambda^2(\tau - \tau') S^2(f - f')}{|\bar{r}_T - \bar{r}|^2 |\bar{r}_R - \bar{r}|^2} d\bar{r} \quad (8)$$

where P_R^{inc} is the incoherent component of received power at delay and Doppler offsets τ and f from the specular point, respectively, σ^0 is the surface normalized bistatic radar cross section (BRCS), and the $(1/R^2)$ terms account for the fall off of power with range on both the transmit and receive paths. Finally, the product of the functions Λ and S accounts for the ambiguity function of the transmit waveform used; the convolution over these functions “smears” the contributions of individual surface points \bar{r} in the integration into the final DDM.

All the quantities included inside the integral vary over earth's surface and therefore should be included in the integration. However, for DDM contributions near the specular points $\tau \approx 0$ and $f \approx 0$, we can further approximate

$$P_R^{\text{inc}}(0, 0) \approx \frac{P_T \lambda^2 G_R G_T}{(4\pi)^3 r_R^2 r_T^2} \cdot \sigma^0 \cdot A_{\text{eff}} \quad (9)$$

under the assumption that the ambiguity function limits contributions for this DDM point to within a small vicinity of the specular point, over which the ranges and antenna gains do not vary appreciably. This approximation is more applicable for higher altitude transmitters and receivers due to the significant variations in angle (and antenna gain) within the first delay-Doppler region that can occur for lower altitudes. The approximation is also more applicable as the signal bandwidth increases, since the resulting smaller sized delay regions limit the angular variation over their extent. Further information on the limits of this approximation will be provided in Sections III and V.

In (9), A_{eff} represents the effective area on the surface corresponding to the ambiguity function integrated over the surface with zero delay and Doppler offset. It can be represented approximately as two-thirds of the area of an elliptical shape defined by semi-major and semi-minor axes G_{1x} and G_{1y} , respectively [26]–[29] that correspond approximately to the delay and Doppler dimensions

$$A_{\text{eff}} = \frac{2\pi}{3} \cdot G_{1x} \cdot G_{1y} = \pi \left(\frac{G_{1m}}{2} \right)^2 \quad (10)$$

The final equality defines an “effective” diameter G_{1m} of A_{eff} that is proportional to the geometric mean of the semi-major and semi-minor axes, G_{1x} and G_{1y} , respectively. The semi-major axis length of the delay ellipse in the scattering plane for a spherical earth can be found as

$$G_{1x} = \frac{1}{D_x \cos \theta} \sqrt{\frac{2c(r_R r_T)}{B(r_R + r_T)}} \quad (11)$$

where c is the speed of light and B represents the bandwidth of the transmitted signal. The influence of the Doppler ambiguity function is dependent on the coherent integration time and the specific transmitter and receiver velocities. Here, it is

characterized as producing a semi-minor axis in the y -direction that is expressed as a multiple of G_{1x}

$$G_{1y} = TG_{1x} \quad (12)$$

with $T = (D_x/D_y) \cos \theta$ in the limit that the delay ambiguity function entirely determines A_{eff} . Given the variation of A_{eff} with the particular scenario considered, the results to follow should be taken only as estimates under typical conditions. Because the goal of this analysis is to obtain basic insights into the importance of coherent effects, this level of accuracy is sufficient.

Finally, for incoherent scattering from a rough surface, the geometrical optics (GO) expression [25] for the specular NRCS is

$$\sigma^0 \approx \frac{|\mathfrak{R}|^2}{s^2} \quad (13)$$

where s^2 is the low-pass-filtered surface mean square slope (MSS). For ocean surfaces, the MSS can be expressed as

$$s^2 = 2s_u s_c \quad (14)$$

within which s_u and s_c are the surface rms slopes in the upwind and crosswind directions, respectively, independent of the orientation of the scattering plane with respect to the wind direction [33]. It is noted that the GO expression provides only a rough approximation for the NRCS at low winds due to the limited applicability of the GO limit of the Kirchhoff approximation for regimes other than strong diffuse scattering [23].

C. Relative Contribution of Coherent Power

Combining (9) and (1), we obtain the ratio K of the coherent to incoherent power as

$$\begin{aligned} K &= P_R^{\text{coh}} / P_R^{\text{inc}} \\ &= 3s^2 \left(\frac{B D_x^2 \cos^2 \theta}{cT} \right) \cdot \frac{r_R r_T}{r_R + r_T} \cdot Z_f \cdot e^{-4k_0^2 h^2 \cos^2 \theta} \end{aligned} \quad (15)$$

$$\approx 3s^2 \cdot \left(\frac{B}{c} \right) \cdot h_R \cdot Z_f \cdot e^{-4k_0^2 h^2 \cos^2 \theta} \quad (16)$$

with the second equation assuming that $r_T \gg r_R$, $D_x \approx 1$, and $T = \cos \theta$, and using the receiver height above the tangent plane at the specular point $h_R = r_R \cos \theta$. The ratio K approximately accounts for the effects of surface roughness, frequency, receiver bandwidth, and the scattering geometry on the relative contribution of the coherent term.

III. APPLICATION TO SPECULAR SCATTERING FROM THE SEA SURFACE

To examine (16) for the sea surface, information on the expected rms height and MSS of the sea surface is required. Given a model of the sea surface power spectral density $\psi(k, \varphi)$ (as, for example, in [34]), the surface height variance can be obtained as

$$h^2 = \int_{\frac{2\pi}{F_{1m}}}^{\infty} \int_{-\pi}^{\pi} \psi(k, \varphi) d\varphi k dk. \quad (17)$$

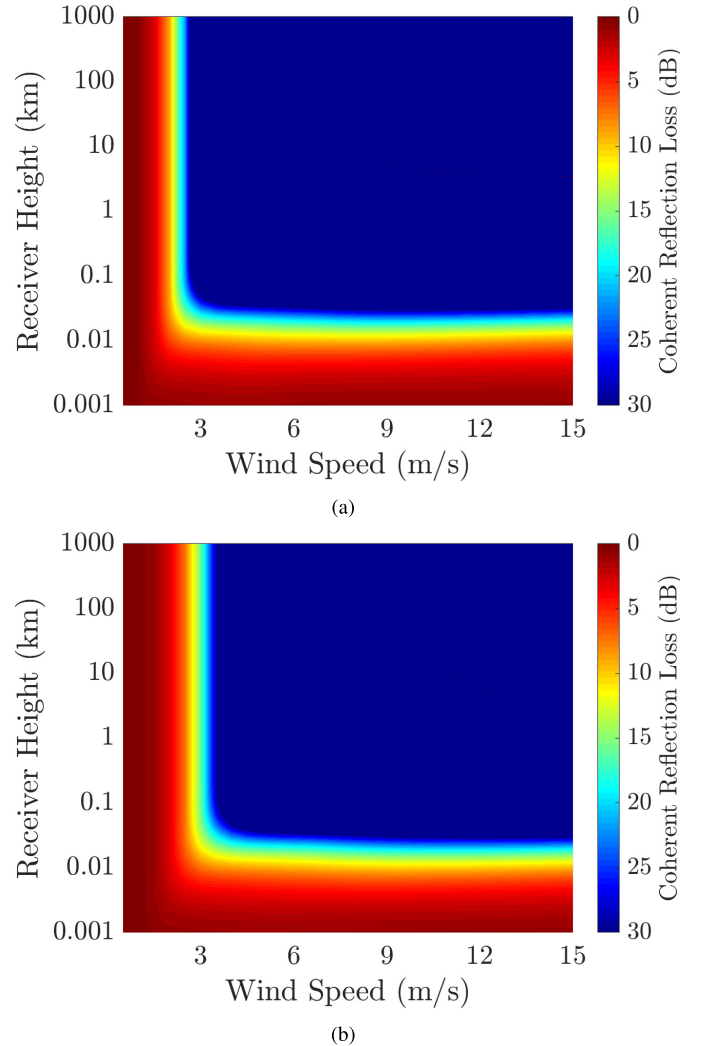


Fig. 4. L-band (1.575 GHz) CRL for varying wind speeds and receiver altitudes at incidence angles (a) $\theta = 30^\circ$ and (b) $\theta = 60^\circ$.

The integration over wavenumber would extend from zero to infinity if the height variance contributions of all sea surface length scales were included. However, the integration here includes only wavenumbers corresponding to length scales smaller than the size of the first Fresnel zone ($2\pi/F_{1m}$). This is because the height variance is used in (16) to compute the roughness-induced reduction of the coherent term, which arises primarily from surface points within the first Fresnel zone. This assumption is reasonable for scenarios in which it can be assumed that surface roughness properties are uniform over large spatial scales (e.g., the sea surface) and would be less applicable to land scenes in which surface roughness properties may vary significantly in space.

Figs. 4 and 5 plot the resulting CRL given by (2) of wind speed and receiver height for the L- (1.575 GHz) and P- (360 MHz [15], [16]) bands, respectively. Plots for incidence angles of $\theta = 30^\circ$ and 60° are included in each case. Note that receiver height enters the computation through its influence on the Fresnel zone size (see Fig. 3) and therefore on the surface height variance computation [see (17)]. These figures illustrate the rapid decrease in the coherent term that occurs as

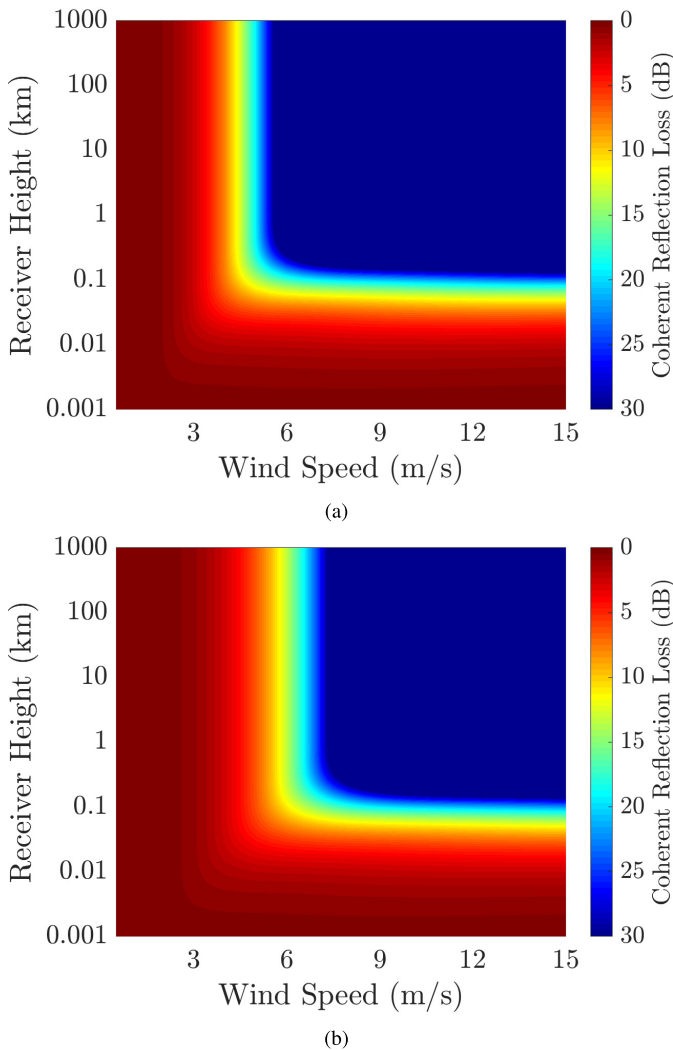


Fig. 5. P-band (360 MHz) CRL for varying wind speeds and receiver altitudes at incidence angles (a) $\theta = 30^\circ$ and (b) $\theta = 60^\circ$.

the wind speed (and height variance) increase, as well as the decreases that occur with receiver height as the Fresnel zone size and corresponding roughness increases. For the L-band at $\theta = 30^\circ$ and receiver heights greater than 100 m, the coherent term attenuates rapidly with wind speed beyond a wind speed of approximately 2 m/s. This boundary is extended slightly to ≈ 3 m/s for the $\theta = 60^\circ$ case. For lower altitude receivers at heights 30 m or less, i.e., ground-based applications [36]–[39], the first Fresnel zone size and surface roughness contained reduce sufficiently to allow coherence for an extended range of wind speeds. Results at the P-band are similar, but show a wider range of wind speeds (up to ≈ 5 –7 m/s for higher altitude receivers) and receiver heights (up to ≈ 100 m) for which coherent returns are expected to be appreciable, due to the reduced impact of surface roughness on lower frequency measurements.

While the behavior of the CRL provides some insight into the relative importance of coherent effects, the full evaluation of the K -factor requires information on the surface slope variance described by (14) that impacts the incoherent term.

The required quantities can be expressed in terms of ψ as

$$s_u^2 = \int_{\frac{2\pi}{G_{1m}}}^{\frac{k_0}{3} \cos \theta} \int_{-\pi}^{\pi} k^3 \cos^2(\varphi) \psi(k, \varphi) d\varphi dk \quad (18)$$

$$s_c^2 = \int_{\frac{2\pi}{G_{1m}}}^{\frac{k_0}{3} \cos \theta} \int_{-\pi}^{\pi} k^3 \sin^2(\varphi) \psi(k, \varphi) d\varphi dk \quad (19)$$

where it is implied that $\varphi = 0^\circ$ in the integration is the upwind direction [34]. In this case, the lower limit of the integration extends to length scales corresponding to the effective incoherent scattering area for the near specular portion of the DDM. The integration upper limit is truncated at the wavenumber corresponding to the short scale “cutoff” wavenumber $(k_0 \cos \theta)/3$ commonly used in the two-scale theory of sea scattering.

Fig. 6 shows K values obtained using (16) together with (17)–(19) as a function of wind speed and receiver altitude for signal bandwidths of 1 MHz at the L-band (the CYGNSS C/A code) and an assumed 0.5 MHz at the P-band. In this case, the axes are restricted to regions for which the angular variation over A_{eff} is small and for which the surface rms height within A_{eff} is sufficient to ensure incoherent scattering. The figures show results similar in nature to those for the CRL, although the case of low altitudes is excluded from the analysis. For the L-band, again wind speeds ≈ 2 –4 m/s (depending on incidence angle) represent the limit beyond which incoherent effects should be expected to dominate observations, while the P-band case shows that coherence can be important up to wind speeds of 6–7 m/s.

While the approach applied remains approximate, it nevertheless provides insight into the importance of coherence over the sea surface. It is noted that CYGNSS measurements have indeed confirmed that coherence can occur for wind speeds less than approximately 2–3 m/s. It is also noted that in such conditions, the surface rms height is likely to be significantly impacted by any contributions from non-local swell that are not captured by standard models for the sea surface power spectrum and its dependence on wind speed alone.

IV. SPECULAR SCATTERING OVER LAND

Several studies analyzing land surface specular scattering from space or airborne measurements [40] have noted the high variability of land returns. Fig. 7 provides an example of CYGNSS NRCS measurements within 50 km of the TxSON measurement site in Texas. The results show an NRCS variability exceeding 10 dB, with the circled points suggesting the presence of coherent reflections from the land surface that are less present at other points in the time series. It is noted that the small size of F_{1m} compared with G_{1m} can result in a significant dependence of the returns on the exact location of the track within the region included in Fig. 7.

Equation (16) can be examined as a function of the surface rms height to obtain some insight into expectations for land surface returns. Fig. 8 plots the K -factor as a function of rms height and incidence angle for a CYGNSS-like measurement (i.e., 1.575 GHz, 1-MHz bandwidth, and $r_R \approx 500$ km $\ll r_T$) and for a P-band system (360 MHz, 0.5-MHz bandwidth, and

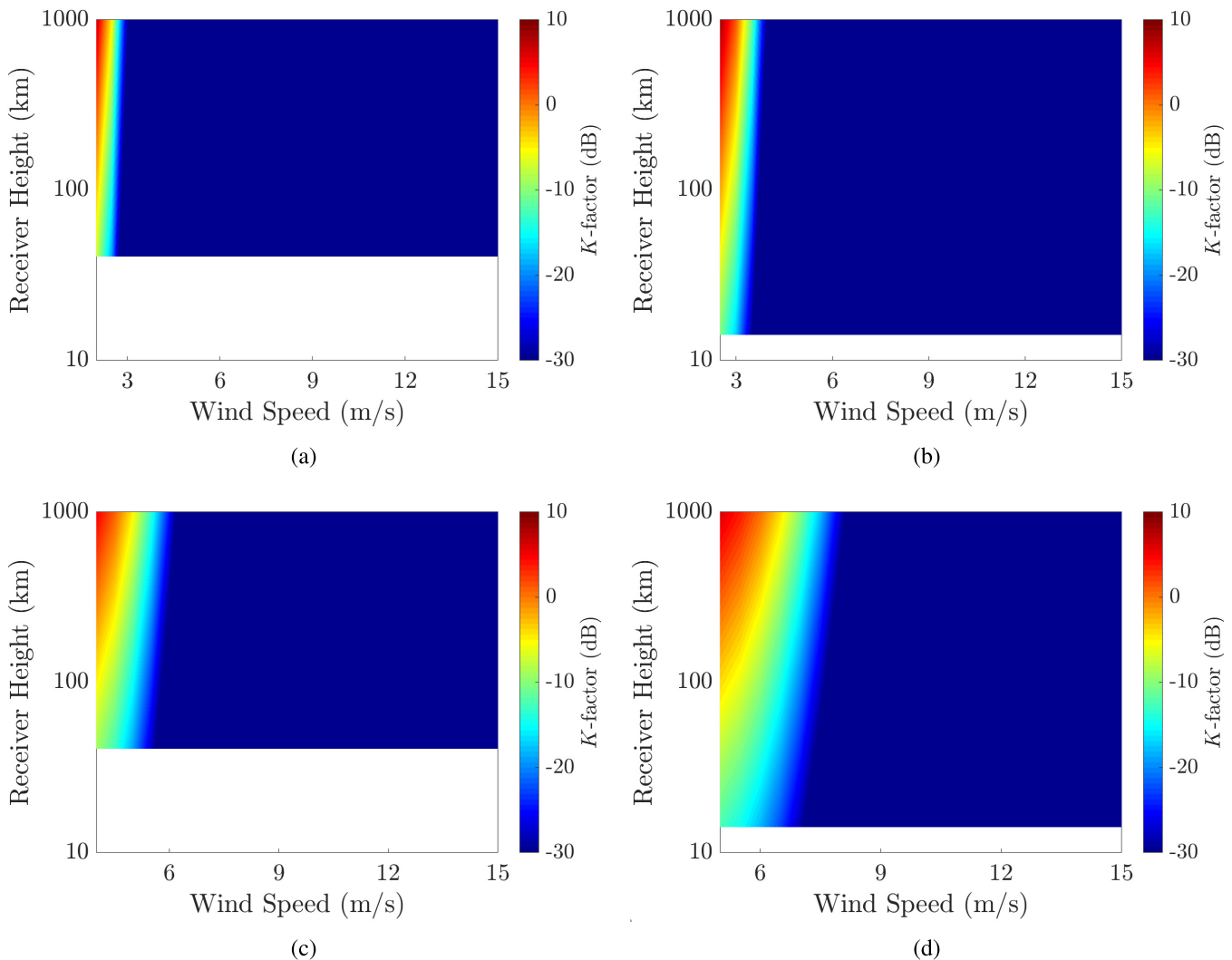


Fig. 6. Depiction of K -factor at varying receiver altitude and surface wind speeds for (a) L-band at $\theta = 30^\circ$, (b) L-band at $\theta = 60^\circ$, (c) P-band at $\theta = 30^\circ$, and (d) P-band at $\theta = 60^\circ$.

similar orbit properties), assuming that $s^2 = 0.01$. For the L-band, the results show a rapid reduction in the importance of coherence for surface rms heights greater than 4–8 cm (as a function of incidence angle) within the first Fresnel zone region. Similar results are reported in [41], where a surface rms height of ≈ 3 cm was reported as the boundary beyond which coherent returns were not observed. The range of rms heights for which coherence is expected at the P-band is expanded by approximately the ratio of the frequencies, but coherence still decreases even in this case for rms heights greater than 15–30 cm.

While models for the roughness of land surfaces are not as readily available as in the sea surface case, Fig. 8 makes clear that terrain rms heights are required to be within a few cm over regions approximately the size of the first Fresnel zone, i.e., hundreds of meters, for the example of CYGNSS. An examination of digital elevation maps over these scales typically shows rms heights on the order of meters, although it is noted that the errors in existing digital elevation maps are large compared to the cm length scales of interest here. Nevertheless, the requirement for terrain heights to be very flat over these scales suggests that land surface coherent returns at

the L-band are most likely to arise from inland water bodies since it is only for such surfaces that rms heights can be assumed to be at the required levels. The prevalence of coherent returns for P-band spaceborne measurements should be expected to be greater than that at L-band, but the assumption that terrain surface rms heights remain within ~ 15 –30 cm over ~ 1 –2-km length scales remains to be validated due to the impact of earth's natural topography over such scales. It is also noted that at the L-band, the penetration depth is limited to near-surface (\approx top 5-cm layer) depths, while at P-band, the reflected wave will also be impacted by any sub-surface layers or volume scattering. Such contributions may further reduce the coherence of P-band returns. Section V further examines the properties of coherent returns from inland water bodies as a function of their boundary shape and any offset from the specular point.

V. IMPACT OF SMOOTH REGION BOUNDARIES ON COHERENT RETURNS

Under the physical optics model of scattering from a rough surface, the electric field scattered from a rough surface has

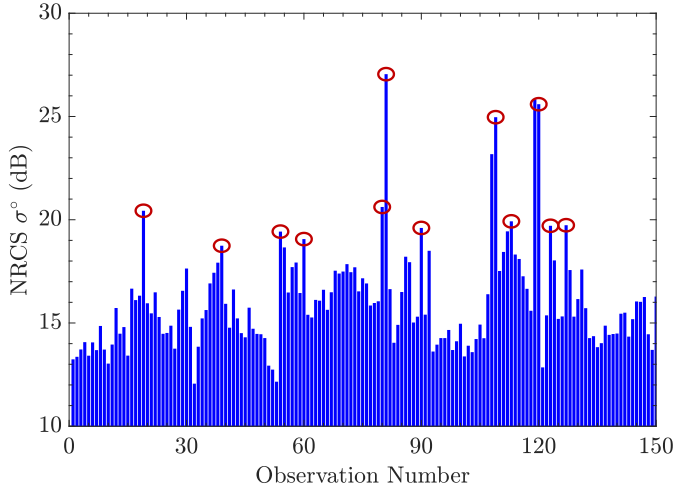


Fig. 7. Example of bistatic land returns (NRCS) derived from CYGNSS constellation CYG01-CYG08 operating at L-band over site of interest (TxSON, TX) within 50-km radius of site location on January 10, 2019. The variability within a relatively small footprint highlights the impact of the presence of very flat surfaces corresponding to inland water bodies.

the form

$$\begin{aligned} \bar{E}_s = \frac{ik_0 \cos \theta}{2\pi} [(\hat{h}_s \hat{h}_i \Gamma_H + \hat{v}_s \hat{v}_i \Gamma_v) \cdot \hat{e}_i] \\ \times \int_A dA \frac{e^{-ik_0 r_{\text{tot}}}}{|\bar{r}_T - \bar{r}| |\bar{r}_R - \bar{r}|} \end{aligned} \quad (20)$$

with (\hat{h}_s, \hat{v}_s) and (\hat{h}_i, \hat{v}_i) representing horizontally and vertically polarized unit vectors for the incident and scattered directions, Γ_h and Γ_v are the Fresnel reflection coefficients for the electric fields, and \hat{e}_i a unit vector representing the incident wave polarization at the specular point. Also, as shown in Fig. 2

$$r_{\text{tot}} = |\bar{r}_T - \bar{r}| + |\bar{r}_R - \bar{r}| \quad (21)$$

with

$$\bar{r}_T = r_T (-\hat{x} \sin \theta + \hat{z} \cos \theta) \quad (22)$$

$$\bar{r}_R = r_R (\hat{x} \sin \theta + \hat{z} \cos \theta) \quad (23)$$

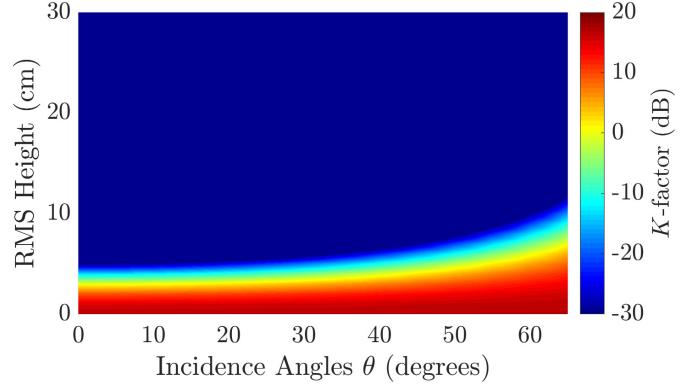
$$\bar{r} = \rho (\hat{x} \cos \phi + \hat{y} \sin \phi) - \hat{z} \frac{\rho^2}{2a_{\text{eff}}} \quad (24)$$

$$= \hat{x}x + \hat{y}y - \hat{z} \frac{\rho^2}{2a_{\text{eff}}} \quad (25)$$

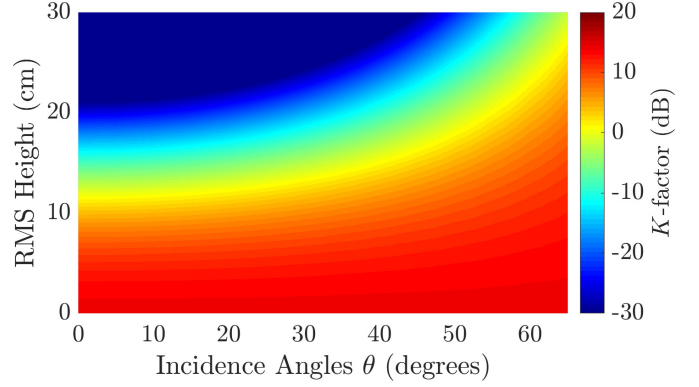
where the final equation assumes that the spherical earth surface has no additional roughness. For a spherical earth surface, the integration over area can be expressed as

$$dA = d\bar{r} \frac{1}{\sqrt{1 - \left(\frac{\rho}{a_{\text{eff}}}\right)^2}} \quad (26)$$

where the area A considered extends only over the “smooth” surface region, e.g., the extent of an inland water body. It is assumed, in what follows, that $\rho \ll a_{\text{eff}}$ so that the term in the square root in (26) is approximated as unity, and that other contributions from earth’s surface are dominated by the contribution of the smooth surface region.



(a)



(b)

Fig. 8. K -factor as a function of rms height and incidence angle. (a) 1.575 GHz. (b) 360 MHz.

Now assuming that $\rho \ll r_R$ and $\rho \ll r_T$, we can approximate

$$\begin{aligned} r_{\text{tot}} \approx r_R + r_T \\ + \rho^2 \left(\frac{r_R + r_T}{2r_R r_T} [\sin^2 \phi + \cos^2 \theta \cos^2 \phi] + \frac{\cos \theta}{a_{\text{eff}}} \right) \end{aligned} \quad (27)$$

$$\begin{aligned} \frac{1}{|\bar{r}_T - \bar{r}|} \approx \frac{1}{r_T} \left\{ 1 - \frac{\rho}{r_T} \sin \theta \cos \phi \right. \\ \left. - \left(\frac{\rho}{r_T} \right)^2 \frac{1 - 3 \sin^2 \theta \cos^2 \phi + \cos \theta \frac{r_T}{a_{\text{eff}}}}{2} \right\} \\ \approx \frac{1}{r_T} \end{aligned} \quad (28)$$

$$\begin{aligned} \frac{1}{|\bar{r}_R - \bar{r}|} \approx \frac{1}{r_R} \left\{ 1 + \frac{\rho}{r_R} \sin \theta \cos \phi \right. \\ \left. - \left(\frac{\rho}{r_R} \right)^2 \frac{1 - 3 \sin^2 \theta \cos^2 \phi + \cos \theta \frac{r_R}{a_{\text{eff}}}}{2} \right\} \\ \approx \frac{1}{r_R}. \end{aligned} \quad (29)$$

It is noted that the third-order term in ρ in (27) (not shown) is equal to the second-order correction multiplied by $\sin \theta (x/M_1)$ when earth curvature is neglected, where M_1 is

$$M_1 = \frac{r_R r_T}{r_T - r_R} \approx r_R \quad (30)$$

with the final form holding for $r_T \gg r_R$. Therefore, higher order corrections become significant only when the smooth region considered has dimensions approaching the distance to the receiver.

Equations (28) and (29) show that it is an acceptable approximation to neglect the dependence on ρ in the terms in the denominator of the integrand in (20). However, the effect of ρ on the phase term must be included as

$$k_0 r_{\text{tot}} \approx k_0(r_R + r_T) + k_0 \rho^2 \left(\frac{r_R + r_T}{2r_R r_T} [\sin^2 \phi + \cos^2 \theta \cos^2 \phi] + \frac{\cos \theta}{a_{\text{eff}}} \right) \quad (31)$$

$$= k_0(r_R + r_T) + \frac{\pi x^2}{F_{1x}^2} + \frac{\pi y^2}{F_{1y}^2} \quad (32)$$

with F_{1x} and F_{1y} accounting for earth curvature effects as defined in (6) and (7).

The integral now has the form

$$\overline{E}_s = \frac{ik_0 \cos \theta e^{-ik_0(r_R+r_T)}}{2\pi r_R r_T} [(\hat{h}_s \hat{h}_i \Gamma_H + \hat{v}_s \hat{v}_i \Gamma_v) \cdot \hat{e}_i] \times \int_A d\vec{r} \exp\left(-i\frac{\pi x^2}{F_{1x}^2}\right) \exp\left(-i\frac{\pi y^2}{F_{1y}^2}\right). \quad (33)$$

A. Smooth Region That Includes the Specular Point

If the substitution $x' = \sqrt{\pi}x/F_{1x}$ and $y' = \sqrt{\pi}y/F_{1y}$ is now made [note this remaps the original smooth region boundaries into the (x', y') space], we obtain

$$\overline{E}_s = \frac{ik_0 \cos \theta e^{-ik_0(r_R+r_T)}}{2\pi r_R r_T} [(\hat{h}_s \hat{h}_i \Gamma_H + \hat{v}_s \hat{v}_i \Gamma_v) \cdot \hat{e}_i] \times \frac{F_{1x} F_{1y}}{\pi} \int_{A'} d\vec{r}' \exp(-i\rho'^2) \quad (34)$$

$$\overline{E}_s = \frac{ie^{-ik_0(r_R+r_T)}}{\pi(r_R + r_T) D_x D_y} [(\hat{h}_s \hat{h}_i \Gamma_H + \hat{v}_s \hat{v}_i \Gamma_v) \cdot \hat{e}_i] \times \int_{A'} d\vec{r}' \exp(-i\rho'^2) \quad (35)$$

$$= Z_f \overline{E}_{f\text{riis}} \quad (36)$$

where the electric field under the Friis formula for a spherical earth is

$$\overline{E}_{f\text{riis}} = \frac{e^{-ik_0(r_R+r_T)}}{D_x D_y (r_R + r_T)} [(\hat{h}_s \hat{h}_i \Gamma_H + \hat{v}_s \hat{v}_i \Gamma_v) \cdot \hat{e}_i].$$

Here

$$Z_f = \frac{i}{\pi} \int_{A'} d\rho' d\phi' \rho' \exp(-i\rho'^2) \quad (37)$$

represents the ratio of the reflected field to that assumed under an infinite spherical flat surface reflection. The expression for $\overline{E}_{f\text{riis}}$ accounts for the reduction in the reflection coefficient caused by earth curvature (through the terms D_x and D_y), while Z_f accounts for impact of the smooth region boundaries through the integration over A' . If the further substitution $q = \rho'^2$ is made, Z_f becomes

$$Z_f = \frac{i}{2\pi} \int_{A''} dq d\phi' \exp(-iq) \quad (38)$$

$$= 1 - \frac{1}{2\pi} \int_0^{2\pi} d\phi' \exp(-i\rho_{\text{max}}'^2(\phi')). \quad (39)$$

It is assumed, in the final expression, that the specular point lies within the smooth surface region, and that the boundary of the smooth surface region can be expressed as $\rho' = \rho'_{\text{max}}(\phi')$. This expression makes clear that Z_f is highly dependent on the boundary shape of the smooth surface region, since it takes the form of a difference between one and an average of equal amplitude phase terms evaluated on the region boundary. For the case of an elliptical disk smooth region $\rho'_{\text{max}}(\phi') = R_{\text{max}}(\sqrt{\pi}/F_{1y})$, Z_f further simplifies to

$$Z_{f,\text{disk}} = \left(1 - \exp\left(-i\pi \left(\frac{R_{\text{max}}}{F_{1y}}\right)^2\right) \right) \quad (40)$$

which again shows the oscillatory properties of Z_f in that the field amplitude can range from zero to approximately twice that predicted by the Friis formula.

For arbitrarily shaped smooth surface regions containing the specular point that are small compared to the Fresnel zone size, the exponential argument inside the integral of (39) can be expanded with the result

$$Z_f \approx \frac{i}{2\pi} \int_0^{2\pi} d\phi' \rho_{\text{max}}'^2(\phi') \quad (41)$$

$$= \frac{iA}{F_{1x} F_{1y}} \quad (42)$$

so that, in the limit of small smooth surface area, the field is proportional to the ratio of the smooth region and Fresnel zone areas. The resulting coherent power is then proportional to the smooth region area squared, so that a rapid increase should be expected with water body size for small water bodies.

B. Rectangular Smooth Surface Region

For the particular case of a rectangular smooth surface region existing between coordinates X_1 and X_2 along x and coordinates Y_1 and Y_2 along y (as shown in Fig. 2), Z_f can be expressed in terms of Fresnel integrals as

$$Z_{f,\text{rect}} = \frac{i}{2} Q\left(\frac{\sqrt{2}x}{F_{1x}}\right)\Bigg|_{X_1}^{X_2} Q\left(\frac{\sqrt{2}y}{F_{1y}}\right)\Bigg|_{Y_1}^{Y_2} \quad (43)$$

where the $|$ notation refers to the difference of the Q function evaluated for x or y , respectively, at the upper and lower limits indicated. Here

$$Q(z) = C(z) - iS(z) = \int_0^z dt e^{-i\frac{\pi t^2}{2}} \quad (44)$$

$$\approx z \quad (45)$$

$$\approx \frac{e^{-i\frac{\pi}{4}}}{\sqrt{2}} \left(1 - \sqrt{2} e^{-i\frac{\pi}{2}} (z^2 - \frac{1}{2}) \frac{z}{1 + i\pi z^2 - \frac{2}{5 + i\pi z^2}} \right) \quad (46)$$

with $C(z)$ and $S(z)$ being the Fresnel integrals and the final two equations holding in the small and large z limits, respectively. If the small argument form is applied in (43), (42) is again obtained. For larger size smooth regions, the large argument form shows an oscillatory behavior in z (i.e., smooth region boundary location) that approaches unity with an oscillation amplitude that decays eventually

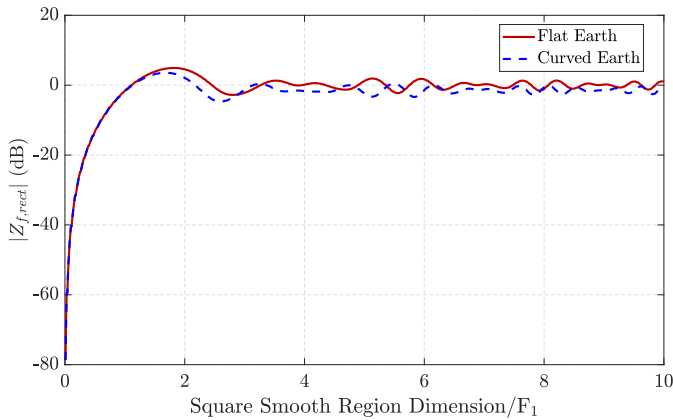


Fig. 9. Coherent power relative to Friis formula for a square smooth region as a function of the square region size with respect to F_1 , for $\theta = 30^\circ$.

as $(1/z)$. For a rectangular smooth surface region centered on the specular point (so that $X_1 = -H/2 = -X_2$ and $Y_1 = -W/2 = -Y_2$ with H and W the height and width of the rectangle), the values of Q evaluated at the boundary limits are equal and opposite, and $Z_{f,rect}$ is proportional to the product of (46) evaluated with $z = (H/\sqrt{2}F_{1x})$ and $z = (W/\sqrt{2}F_{1y})$.

Fig. 9 shows the amplitude of $Z_{f,rect}$ as a function of the size of a square region centered on the specular point for a CYGNSS like observation at $\theta = 30^\circ$. Curves are included for the cases in which earth curvature is included or neglected, with the results showing that earth curvature can make a small but appreciable impact particularly on the oscillatory pattern observed [note the horizontal axis is scaled in both the cases in terms of the Fresnel zone size neglecting earth curvature from (3)]. The results show the rapid increase in received power as the smooth region size increases [as predicted in (42)], followed by the oscillatory pattern versus boundary size for which the oscillations decay with F_{1x}/H and F_{1y}/W . While the oscillatory pattern is not as dramatic as that for the elliptical disk, the fluctuations observed nevertheless highlight the sensitivity of coherent reflections to the specific shape of the smooth region encountered. Results were also compared between the complete evaluation of (20) and the approximated version (43) and found to be indistinguishable.

Finally, (43) is applied to the case of a rectangular region shifted from the specular point, e.g., $X_1 = x_c - H/2$, $X_2 = x_c + H/2$, $Y_1 = y_c - W/2$, and $Y_2 = y_c + W/2$. For a rectangle with a small height (H) and width (W) compared to the respective Fresnel zone sizes, it can be shown for small (x_c, y_c) that the resulting field still follows (42) but with a phase shift corresponding to the modified smooth region center location. Alternately, for smooth region boundaries that are shifted significantly away from the specular point in terms of the Fresnel zone dimensions, the approximation

$$Q(z+\Delta) - Q(z-\Delta) \approx \frac{2}{\pi} e^{-i\frac{\pi}{2}(z^2+\Delta^2)} \frac{\sqrt{z^2+\Delta^2}}{z^2-\Delta^2} \times (\cos \alpha \sin \beta - i \sin \alpha \cos \beta) \quad (47)$$

$$\cos \alpha = \frac{z}{\sqrt{z^2+\Delta^2}} \quad (48)$$

$$\beta = \pi x \Delta \quad (49)$$

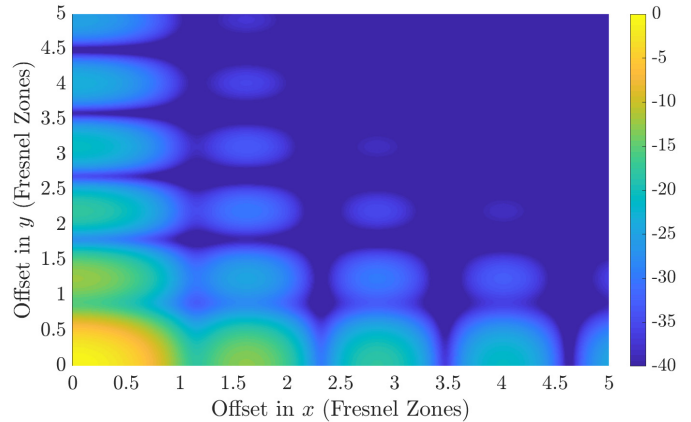


Fig. 10. Coherent power relative to Friis formula for a square smooth region of side length F_1 as a function of the center region offset from the specular point, for $\theta = 30^\circ$.

can be developed from (46). For center offsets that are large compared to the smooth region dimensions, α will be small and the second term in the parenthesis can be neglected except for cases when $\sin \beta$ approaches zero. This approximation makes clear that oscillatory behaviors are still obtained as a function of either smooth region offset or smooth region size and that the amplitude of the coherent field decays approximately as one over the center offset normalized by the corresponding Fresnel zone size.

Fig. 10 shows the amplitude of $Z_{f,rect}$ for a smooth region of size F_1 by F_1 as a function of the center offset in x and y from the specular point, for $\theta = 30^\circ$ and a CYGNSS-like geometry. The results show the expected oscillations as well as the reduction in amplitude of the coherent field as the smooth region center is moved from the specular point. Again, these results highlight the significant variability that can occur in coherent fields as a function of their precise shape and location with respect to the specular point.

VI. CONCLUSION

The model presented in this article provides a simple methodology for assessing the expected importance of coherent contributions for both land and ocean surfaces. This is described as a function of frequency, bandwidth, observing geometry, and surface properties. Application of the model to the L- and P-band examples showed that coherent contributions over sea surfaces should occur infrequently at the L-band and at the P-band (360 MHz) up to wind speeds of 6–8 m/s. An analysis of land surface returns at the L-band showed that inland water bodies are likely to be the primary factor producing coherent returns over land. This is due to the small rms heights that are required over length scales up to hundreds of meters in order to retain coherence. The prevalence of coherent returns for P-band spaceborne observations should be greater, but terrain surfaces with rms heights less than approximately 15–30 cm will still be required over length scales of ~ 1 –2 km on earth's surface. The analysis presented for coherent returns from inland water bodies showed the significant variability that should be expected as a function of smooth region shape and offset from the specular point.

Such returns are also influenced by any small-scale roughness on the smooth region surface, adding further variability. Attempts to use the amplitudes of coherent GNSS-R returns to retrieve properties of inland water bodies will therefore need to account for these effects.

ACKNOWLEDGMENT

The authors would like to thank NASA EOSDIS Physical Oceanography Distributed Active Archive Center (PO.DAAC), Jet Propulsion Laboratory, Pasadena, CA, USA, for making GNSS-R data derived from the CYGNSS constellation available.

REFERENCES

- [1] M. P. Clarizia and C. S. Ruf, "Wind speed retrieval algorithm for the cyclone global navigation satellite system (CYGNSS) mission," *IEEE Trans. Geosci. Remote Sens.*, vol. 54, no. 8, pp. 4419–4432, Aug. 2016.
- [2] *CYGNSS Handbook, Cyclone Global Navigation Satellite System: Deriving Surface Wind Speeds in Tropical Cyclones*, Univ. Michigan, Ann Arbor, MI, USA, 2016.
- [3] C. C. Chew and E. E. Small, "Soil moisture sensing using spaceborne GNSS reflections: Comparison of CYGNSS reflectivity to SMAP soil moisture," *Geosci. Res. Lett.*, vol. 45, no. 9, pp. 4049–4057, 2018.
- [4] M. M. Al-Khalidi, J. Johnson, A. J. O'Brien, A. Balenzano, and F. Mattia, "Time-series retrieval of soil moisture using CYGNSS," *IEEE Trans. Geosci. Remote Sens.*, vol. 57, no. 7, pp. 4322–4331, Jul. 2019.
- [5] H. Carreno-Luengo, S. Lowe, C. Zuffada, S. Esterhuizen, and S. Oveisgharan, "Spaceborne GNSS-R from the SMAP mission: First assessment of polarimetric scatterometry over land and cryosphere," *Remote Sens.*, vol. 9, no. 4, p. 362, Apr. 2017.
- [6] H. Carreno-Luengo, A. Camps, J. Querol, and G. Forte, "First results of a GNSS-R experiment from a stratospheric balloon over boreal forests," *IEEE Trans. Geosci. Remote Sens.*, vol. 54, no. 5, pp. 2652–2663, May 2016.
- [7] M. Al-Khalidi, J. T. Johnson, J. Park, and A. O'Brien, "An analysis of CYGNSS returns over land," *USNC-URSI Nat. Radio Sci. Meeting*, Boulder, CO, USA, Jan 2018.
- [8] M. Al-Khalidi, J. T. Johnson, A. O'Brien, F. Mattia, and A. Balenzano, "GNSS-R time-series soil moisture retrievals from vegetated surfaces," in *Proc. IEEE Int. Geosci. Remote Sens. Symp. (IGARSS)*, Valencia, Spain, Jul. 2018, pp. 2035–2038.
- [9] W. Li, A. Rius, F. Fabra, E. Cardellach, S. Ribó, and M. Martín-Neira, "Revisiting the GNSS-R waveform statistics and its impact on altimetric retrievals," *IEEE Trans. Geosci. Remote Sens.*, vol. 56, no. 5, pp. 2854–2871, May 2018.
- [10] A. Alonso-Arroyo, V. U. Zavorotny, and A. Camps, "Sea ice detection using U.K. TDS-1 GNSS-R data," *IEEE Trans. Geosci. Remote Sens.*, vol. 55, no. 9, pp. 4989–5001, Sep. 2017. doi: [10.1109/tgrs.2017.2699122](https://doi.org/10.1109/tgrs.2017.2699122).
- [11] J. Wickert *et al.*, "GEROS-ISS: GNSS reflectometry, radio occultation, and scatterometry onboard the international space station," *IEEE J. Sel. Topics Appl. Earth Observ. Remote Sens.*, vol. 9, no. 10, pp. 4552–4581, Oct. 2016. doi: [10.1109/jstars.2016.2614428](https://doi.org/10.1109/jstars.2016.2614428).
- [12] E. Cardellach *et al.*, "Consolidating the precision of interferometric GNSS-R ocean altimetry using airborne experimental data," *IEEE Trans. Geosci. Remote Sens.*, vol. 52, no. 8, p. 4992–5004, Aug. 2014.
- [13] J. S. Löfgren, R. Haas, H.-G. Scherneck, and M. S. Bos, "Three months of local sea level derived from reflected GNSS signals," *Radio Sci.*, vol. 46, no. 6, 2011, Art. no. RS0C05.
- [14] F. Martin *et al.*, "Mitigation of direct signal cross-talk and study of the coherent component in GNSS-R," *IEEE Geosci. Remote Sens. Lett.*, vol. 12, no. 2, pp. 279–283, Feb. 2015.
- [15] J. Knuble *et al.*, "Airborne P-band Signal of Opportunity (SoOP) demonstrator instrument; status update," in *Proc. IEEE Int. Geosci. Remote Sens. Symp. (IGARSS)*, Jul. 2016, pp. 5638–5641.
- [16] S. Yueh *et al.*, "UAS-based P-band signals of opportunity for remote sensing of snow and root zone soil moisture," *Sensors, Syst., Next-Gener. Satell.*, vol. 10785, Sep. 2018, Art. no. 107850B.
- [17] R. Shah, J. L. Garrison, A. Egado, and G. Ruffini, "Bistatic radar measurements of significant wave height using signals of opportunity in L-, S-, and Ku-bands," *IEEE Trans. Geosci. Remote Sens.*, vol. 54, no. 2, pp. 826–841, Feb. 2016.
- [18] S. C. Ho *et al.*, "Wideband ocean altimetry using Ku-band and K-band satellite signals of opportunity: Proof of concept," *IEEE Geosci. Remote Sens. Lett.*, vol. 16, no. 7, pp. 1012–1016, Jul. 2019.
- [19] R. Shah and J. L. Garrison, "Precision of Ku-band reflected signals of opportunity altimetry," *IEEE Geosci. Remote Sens. Lett.*, vol. 14, no. 10, pp. 1840–1844, Oct. 2017.
- [20] V. U. Zavorotny and A. G. Voronovich, "Scattering of GPS signals from the ocean with wind remote sensing application," *IEEE Trans. Geosci. Remote Sens.*, vol. 38, no. 2, pp. 951–964, Mar. 2000.
- [21] A. G. Voronovich and V. U. Zavorotny, "Bistatic radar equation for signals of opportunity revisited," *IEEE Trans. Geosci. Remote Sens.*, vol. 56, no. 4, pp. 1959–1968, Apr. 2018. doi: [10.1109/TGRS.2017.2771253](https://doi.org/10.1109/TGRS.2017.2771253).
- [22] S. Gleason, *Algorithm Theoretical Basis Document (ATBD): Level 1B DDM Calibration*, document 148-0137, Univ. Michigan, Ann Arbor, MI, USA, 2018.
- [23] A. G. Voronovich and V. U. Zavorotny, "The transition from weak to strong diffuse radar bistatic scattering from rough ocean surface," *IEEE Trans. Antennas Propag.*, vol. 65, no. 11, pp. 6029–6034, Nov. 2017.
- [24] C. Levis, F. L. Teixeira, and J. T. Johnson, *Radiowave Propagation: Physics and Applications*. Hoboken, NJ, USA: Wiley, 2010.
- [25] J. T. Johnson, K. F. Warnick, and P. Xu, "On the geometrical optics (Hagfors' law) and physical optics approximations for scattering from exponentially correlated surfaces," *IEEE Trans. Geosci. Remote Sens.*, vol. 45, no. 8, pp. 2619–2629, Aug. 2007.
- [26] S. J. Katzberg and J. L. Garrison, "Utilizing GPS to determine the ionospheric delay over the ocean," NASA, Washington, DC, USA, Tech. Rep. TM-4750, Dec. 1996.
- [27] S. J. Katzberg, O. Torres, M. S. Grant, and D. Masters, "Utilizing calibrated GPS reflected signals to estimate soil reflectivity and dielectric constant: Results from SMEX02," *Remote Sens. Environ.*, vol. 100, no. 1, pp. 17–28, Jan. 2006.
- [28] D. Masters, P. Axelrad, and S. Katzberg, "Initial results of land-reflected GPS bistatic radar measurements in SMEX02," *Remote Sens. Environ.*, vol. 92, no. 4, pp. 507–520, Sep. 2004.
- [29] S. Gleason, "Remote sensing of ocean, ice and land surfaces using bistatically scattered GNSS signals from low earth orbit," Ph.D. dissertation, Univ. Surrey, Guildford, U.K., 2006.
- [30] P. Beckmann and A. Spizzichino, *The Scattering of Electromagnetic Waves From Rough Surfaces*. Norwood, MA, USA: Artech House, 1963.
- [31] D. E. Barrick and W. H. Peake, "Scattering from surfaces with different roughness scales: Analysis and interpretation," Battelle Memorial Inst. Columbus LABS, Columbus, OH, USA, Tech. Rep. BAT-197A-10-3, 1967.
- [32] S. O. Rice, "Reflection of electromagnetic waves from slightly rough surfaces," *Commun. Pure Appl. Math.*, vol. 4, nos. 2–3, pp. 351–378, Aug. 1951.
- [33] J. Park and J. T. Johnson, "A study of wind direction effects on sea surface specular scattering for GNSS-R applications," *IEEE J. Sel. Topics Appl. Earth Observ. Remote Sens.*, vol. 10, no. 11, pp. 4677–4685, Nov. 2017.
- [34] T. Elfouhaily, B. Chapron, K. Katsaros, and D. Vandemark, "A unified directional spectrum for long and short wind-driven waves," *J. Geophys. Res.*, vol. 102, no. C7, pp. 15781–15796, 1997.
- [35] T. M. Elfouhaily and J. T. Johnson, "A new model for rough surface scattering," *IEEE Trans. Geosci. Remote Sens.*, vol. 45, no. 7, pp. 2300–2308, Jul. 2007.
- [36] H. Carreno-Luengo, A. Camps, I. Ramos-Pérez, and A. Rius, "Experimental evaluation of GNSS-reflectometry altimetric precision using the P(Y) and C/A signals," *IEEE J. Sel. Topics Appl. Earth Observ. Remote Sens.*, vol. 7, no. 5, pp. 1493–1500, May 2014.
- [37] N. Rodriguez-Alvarez *et al.*, "Soil moisture retrieval using GNSS-R techniques: Experimental results over a bare soil field," *IEEE Trans. Geosci. Remote Sens.*, vol. 47, no. 11, pp. 3616–3624, Nov. 2009.
- [38] M. B. Rivas and M. Martín-Neira, "Coherent GPS reflections from the sea surface," *IEEE Geosci. Remote Sens. Lett.*, vol. 3, no. 1, pp. 28–31, Jan. 2006.
- [39] A. M. Balakhder, M. Al-Khalidi, and J. T. Johnson, "A study of the amplitude distribution of near-specular bistatic sea clutter," in *Proc. Int. Conf. Electromagn. Adv. Appl. (ICEAA)*, Cartagena, CO, USA, Sep. 2018.
- [40] A. Camps *et al.*, "Sensitivity of GNSS-R spaceborne observations to soil moisture and vegetation," *IEEE J. Sel. Topics Appl. Earth Observ. Remote Sens.*, vol. 9, no. 10, pp. 4730–4742, Oct. 2016.
- [41] A. Egado *et al.*, "Airborne GNSS-R polarimetric measurements for soil moisture and above-ground biomass estimation," *IEEE J. Sel. Topics Appl. Earth Observ. Remote Sens.*, vol. 7, no. 5, pp. 1522–1532, May 2014.

- [42] R. D. De Roo and F. T. Ulaby, "Bistatic specular scattering from rough dielectric surfaces," *IEEE Trans. Antennas Propag.*, vol. 42, no. 2, pp. 220–231, Feb. 1994.
- [43] J. T. Johnson and J. D. Ouellette, "Polarization features in bistatic scattering from rough surfaces," *IEEE Trans. Geosci. Remote Sens.*, vol. 52, no. 3, pp. 1616–1626, Mar. 2014.
- [44] J. L. Garrison, S. J. Katzberg, and M. I. Hill, "Effect of sea roughness on bistatically scattered range coded signals from the global positioning system," *Geophys. Res. Lett.*, vol. 25, no. 13, pp. 2257–2260, Jul. 1998.
- [45] J. L. Garrison, A. Komjathy, V. U. Zavorotny, and S. J. Katzberg, "Wind speed measurement using forward scattered GPS signals," *IEEE Trans. Geosci. Remote Sens.*, vol. 40, no. 1, pp. 50–65, Jan. 2004.
- [46] H. Li and J. T. Johnson, "On the amplitude distributions of bistatic scattered fields from rough surfaces," *IEEE Trans. Geosci. Remote Sens.*, vol. 55, no. 12, pp. 6883–6892, Dec. 2017.



Ahmed M. Balakhder (M'14) received the bachelor's degree in electrical engineering from King Abdulaziz University, Jeddah, Saudi Arabia, in 2009, and the M.S. degree in electrical and computer engineering from The Ohio State University, Columbus, OH, USA, in 2015, where he is currently pursuing the Ph.D. degree with the ElectroScience Laboratory, Department of Electrical and Computer Engineering.

Since 2009, he has been a Researcher with King Abdulaziz City for Science and Technology (KACST), Riyadh, Saudi Arabia. His research interests include radar signal processing, sea clutter analysis, rough surface scattering, and remote sensing.



Mohammad M. Al-Khalidi (M'18) received the bachelor's degree in electrical engineering from the American University of Sharjah, Sharjah, United Arab Emirates, in 2015, the M.S. degree in electrical engineering from Texas A&M University, College Station, TX, USA, in 2017, and the M.S. degree in electrical and computer engineering from The Ohio State University, Columbus, OH, USA, in 2019, where he is pursuing the Ph.D. degree with the ElectroScience Laboratory, Department of Electrical and Computer Engineering.

He is currently a Graduate Research Associate with the ElectroScience Laboratory, Department of Electrical and Computer Engineering, The Ohio State University. His research interests include applied electromagnetics, rough surface scattering, and spaceborne remote sensing.



Joel T. Johnson (S'88–M'96–F'08) received the bachelor's degree in electrical engineering from the Georgia Institute of Technology, Atlanta, GA, USA, in 1991, and the M.S. and Ph.D. degrees from the Massachusetts Institute of Technology, Cambridge, MA, USA, in 1993 and 1996, respectively.

He is currently a Professor with the ElectroScience Laboratory, Department of Electrical and Computer Engineering, The Ohio State University, Columbus, OH, USA. His research interests include microwave remote sensing, propagation, and electromagnetic wave theory.

Dr. Johnson is a member of Commissions B and F of the International Union of Radio Science (URSI) and a member of Tau Beta Pi, Eta Kappa Nu, and Phi Kappa Phi. He was a recipient of the 1993 Best Paper Award from the IEEE Geoscience and Remote Sensing Society, the National Science Foundation Career Award, and the PECASE Award in 1997. He was named an Office of Naval Research Young Investigator. He was recognized by the U.S. National Committee of URSI as a Booker Fellow in 2002.